7

Physical and Optical Properties of Microscale Meshes of Ti_3O_5 Nano- and Microfibers Prepared via Annealing of C-Doped TiO_2 Thin Films Aiming at Solar Cell and Photocatalysis Applications

N. Stem[1], E. F. Chinaglia[2] and S. G. dos Santos Filho[1]
[1]*Universidade de São Paulo/ Escola Politécnica de Engenharia Elétrica (EPUSP)*
[2]*Centro Universitário da FEI/ Departamento de Física*
Brazil

1. Introduction

Dye-sensitized nanocrystalline solar cells (DSSC) or photoeletrochemical solar cells were firstly described by Gratzel and O'Reagan in the early 1990s (Sauvage et. al., 2010) and they have reached the global photovoltaic market since 2007. Later on, the investments in nanotechnology enabled the rapid development of DSSC cells with nanostructured thin films. According to a review performed by Hong Lin et. al. (Lin et. al., 2009) the numbers of papers focusing on the development of the DSSC cells increased in last decade, being mainly originated in countries such as Japan, China, South Korea, Swiss and USA, where there is an enlarged integration of nanotechnology, electrochemical and polymers research and finantial supported projects like National Photovoltaic Program by Department of Energy (DOE) and NEDO's New Sunshine from USA and Japan, respectively. Some research groups of the institutions (Kim et. Al., 2010),which have recently obtained efficiencies around 10%, are EPFL (11.2% in 2005) and AIST (10% in 2006). They have used the N719 colorant in devices with area 0.16cm² and 0.25cm². On the other hand, Sharp, Tokyo University and Sumitomo Osaka Cell have used the black dye colorant in devices with areas of approximately 0.22cm², providing the efficiencies of about 11.1%, 10.2% and 10% in the years 2006, 2006 and 2007, respectively. In 2006, Tokyo University has also reached the efficiency of 10.5% in devices with 0.25cm² area, but using β-diketonide colorant.

Initially, the DSSC (Sauvage et. al., 2010) were based on a nanocrystalline semiconductor (pristine titanium dioxide) coated with a monolayer of charge-transfer dye, with a broad absorption band (generally, polypyridyl complexes of ruthenium and osmium), to sensitize the film. The principle of operation of these devices can be divided into: a) the photo-current generation that occurs when the incident photons absorbs in the dye, generates electron-hole pairs and injects electrons into the conduction band of the semiconductor (Ru^{2+} -> Ru^{3+} + e^-), and b) the carrier transport that occurs because of the migration of these electrons through the nanostructured semiconductor to the anode (Kim et. al., 2010). Thus, since this device requires an electrode with a conduction band with a lower level than the dye one, the

main desired properties for the electrode are optimized band structure and good electron injection efficiency and diffusion properties (Wenger, 2010).
Since Ru has become scarce and its purification and synthesis is too complex for production in large scale, new outlets for doping the titanium dioxide became necessary. Among the materials usually adopted for the electrode, TiO_2, ZnO, SnO_2, Nb_2O_5 and others have been employed (Kong et al., 2007), besides nanostructured materials. For instance, in a previous work, H. Hafez et. al. (Hafez et. al., 2010) made a comparison between the J-V curves of three different structures for the TiO_2 electrodes combined with N719 dye for dye-sensitized cells: a) pure nanorod with adsorbed dye of $2.1x\ 10^{-5}mol.cm^{-2}$; b) pure nanoparticle with adsorbed dye of $3.6x10^{-5}mol.cm^{-2}$ and c) a mix between nanorods and nanoparticles with adsorbed dye of $6.2x10^{-5}mol.cm^{-2}$. These cells presented the incident photon-to-current conversion efficiency, IPCE (at λ=575nm) of approximately 63.5%, 70.0% and 88.9%, and the efficiencies, 4.4%; 5.8% and 7.1%, respectively. A higher efficiency of 7.1% was found for a mixed structure of nanorods and nanoparticles and the efficiencies found for either pure nanoparticules or nanorods were around 5.8% and 4.4%, respectively.
Despite showing lower efficiency compared with the crystalline silicon solar cells, this thin film technology has been pointed as a potential solution to reduce costs of production. Also, they can be engineered into flexible sheets and are mechanically robust, requiring no special protection from environmental events like hail strikes. Other major points of DSSC technology is the fact that it is less sensitive to impurities compared with the conventional crystalline ones because the constituents used are low cost and abundant. Furthermore, differently from the Si-based modules, the performance of dye PV modules increases with temperature. For instance, comparing the Si-based modules with the dye PV modules, Pagliaro et. Al. (2009) showed for temperature variying from 25°C to 60°C that the percentage of power efficiency decreased approximately 40% for the silicon-based one and increased approximately 30% for the STI titania cells (Pagliaro et. al., 2009). Another important characteristic is associated with the color that can vary by changing the dye, being possible to be transparent, which is useful for application on windows surface. However, degradation under heat and UV light are the main disavantages and, in addition, the sealing can also be a problem because of the usage of solvents in the assembling, which makes necessary the development of some gelators combined with organic solvents. The stability of the devices is another important parameter to be optimized (Fieggemeier et. al., 2004), and the competitive light-to-energy conversion efficiencies must be tested. Recently, Wang et. al. (Wang et. al., 2003) have proved that it is possible to keep the device stable under outdoor conditions during 10 years in despite of the complexity of the system.

2. An overview of the techniques for producing titanium oxide nanofibers

The study of titania nanotubes (Ou & Lien, 2007) started in the nineties, with the development of the formation parameters of several processes (temperature, time interval of treatment, pressure, Ti precursors and alkali soluters, and acid washing). With the evolution of the characterization techniques, the thermal and post-thermal annealings were studied, and optimized for the several types of applications (photocatalysis, littium battery, and dye sensitized solar cells). The hydrothermal treatments have also been modificated either physically or chemically depending on the desired application and on the desired stability after post-hydrothermal treatment and post-acid treatments.
Focusing on nanostructured materials developed for solar cells and photocatalysis, titanium dioxide (TiO_2) is one of the most promising due to its high efficiency, low cost and

photostability (Kim et. al. , 2007) (Varghese et. al., 2003). Some resources have been used for enlarging efficiency and for reducing costs. The enhanced porosity of the nanofibers, nanobelts or nanorods of these new structures, which can be used as photoanodes, were proved to have a better response than titanium-dioxide nanoparticles, because of their structure that facilitates the chemical adsorption for polymer electrolytes (Varghese et. al., 2003). There is a wide variety of methods for producing nanofibers and nanotubes techniques, such as sol-gel techniques combined with low cost processes such as arc-plasma evaporation, electrospinning techniques, and hydrothermal methods (Chen and Mao, 2007), (Nuansing et. al., 2006) and (Park et. al., 2010) .

Another resource usually used for enhancing efficiency is the doping (Chennand and Mao, 2007) (Valentini et. al., 2005) , either with non-metallic elements (N, C, S or P) or halogens, in order to reduce bandgap and to shift the adsorption band edge to the visible-light range. And, for producing nanostructured materials, several precursor seeds have been successfully used including alkalines (Kukovecz et. al., 2005), carbon (Puma et. al., 2008) and (Varghese et. al., 2003) and water vapor (Yamamoto et. al., 2008), which also have the role as dopants. For instance, Khan et. al. (Khan et. al., 2009) showed that hydrothermally synthesized titanium dioxide doped with Ru, provided a significantly decrease in the energy bandgap and showed an increase (>80% higher after 140min) in their photocatalytic activity to degrade methylene blue (MB) under visible light compared with undoped tubes. Concomitantly, Zhang et. al. (Zhang et. al., 2010) report the doping of TiO_2 with transition metal ions, specially Fe(III) and Cr(III) as a good tool for improving photocatalytic properties.

According to previous works (Reyes-Garcia et. al., 2009) (Konstantinova et al., 2007), concerning with photocatalytic properties, carbon has been shown as one of the most proeminent dopant for titanium dioxide because it can provide a significant reduction of the optical band gap and the appearance of some C states in the mid-gap. For example, the energy of oxygen vacancies can be reduced from 4.2eV to 3.4eV (interstitional position in the titanium dioxide lattice) and to 1.9eV (substitutional one) for anatase phase and, from 4.4eV to 2.4eV for rutile phase for both positions, interstitial and substitutional. As a result, it has been showed that the photosensitization property is enhanced (Valentini et. al., 2005).

The hydrothermal route and calcination have been the most used techniques by varying time, atmosphere and temperature of annealing. In a previous work (Suzuki & Yoshikawa, 2004) , nanofibers of TiO_2 were synthesized by hydrothermal method (150 ^oC for 72 h) using natural rutile sand as the starting material and calcination at 700^oC for 4 h. On the other hand, pure rutile phase TiO_2 nanorods (Chen et al., 2011) were also successfully synthesized under hydrothermal conditions, showing an increase of the photocatalytic activity for the times ranging from 1 to 15h because of the increase of the crystal domain. The best performance of DSSC measured under "1 sun condition" gave a current density <7.55 mA/cm^2, an open circuit voltage <0.70V, a fill factor <60%, and an energy conversion efficiency <3.16%. Meanwhile, Hafez et. al. (Hafez et. al., 2010) processed anatase TiO_2 nanorods by hydrothermal method and proved that the efficiency could increase from 5.8% to 7.1% if the DSSC electrodes were changed from nanoparticles to nanorods (Wang et. al., 2003). Wu et. al. (2009) proved that the use of ethanol as precursor for producing H-titanate nanotubes in inert N_2 atmosphere. Depending on the calcination temperature, the nanostructure could be altered, presenting either nanotubes, or nanowires or nanorods for calcination temperatures of 400^oC, 500^oC and 600^oC, respectively. It is believed that during the calcination in N_2, the decomposed products of ethanol were not burnt out because there

was not observed oxygen in the environment. Thus, the residual carbon either remainded in the TNTs or it doped the titanium dioxide by forming different nanostructures and, therefore, acting as seeds. Tryba (Tryba, 2008) has also demonstrated that the carbon-based coating of TiO_2, prepared by the calcination of TiO_2 with carbon precursor (polyvinylalcohol, poly (terephthalate ethylene), or hydroxyl propyl cellulose (HPC)) at high temperatures 700◦C – 900◦C retarded the phase transformation from anatase to rutile and increased the photoactivity, but the carbon coating reduced the UV radiation once it reached the surface of the TiO_2 particles and altered the absorbed light.

This work is focused on the development of new technique for producing carbon-doped TiO_2 thin films on silicon substrates together with Ti_3O_5 fiber meshes and on the investigations about the properties of this novel material. The innovation of the proposed technique relies on the fact that thermal evaporation is the most common method to fabricate single crystalline nanowires on silicon substrate by means of the Vapor-Liquid-Solid (VLS) mechanism (Dai et. al., 2002), (Yin et. al., 2002) and (Pan et. al., 2001). On the other hand, it is not an useful process for growing TiO_2 nanowires because Ti precursor can react with silicon to form Ti-Si alloys before nucleation and growth of TiO_2 nanowires (Wu et. al., 2005). Also, it is too difficult the production of titania nanowires by thermal treatment of Ti on Si substrate because $TiSi_2$ phases is favored before nucleation of titanium oxide nanowires in inert gas or high vaccum (Xiang et. al., 2005). On the other hand, a recent study has shown that single crystalline rutile TiO_2 nanowires could be obtained by annealing TiO_2 nanoparticles on silicon substrates at high temperature in air without catalysts (Wang et. al., 2009). Although it is possible to obtain titania nanowires on silicon by thermal annealing, there is a complete lack of information in literature about the effect of carbon as dopant on the physical and electrical properties of TiO_2 nanowires produced by thermal annealing of TiO_2 on silicon substrates. C-doped TiO_2 can evolve to lower oxides of titanium like Ti_4O_7, Ti_3O_5, and Ti_2O_3 after thermal annealing at 1000-1100°C in vacuum or argon. This process is known as carbothermal reduction of titanium dioxide in presence of carbon and can produce TiC powders of submicron size at a very high temperature of 1500°C (Sen et. al, 2011) and (Swift & Koc, 1999).

Thus , in the following, the formation mechanism of nano- and microfibers of Ti_3O_5 produced by annealing of carbon-doped TiO_2 thin films on silicon substrates at 900-1000°C for 120min in wet $N_2(0.8\%H_2O)$ is presented. The effects of concentration of carbon, concentration of water vapor and temperature on the formation of the nano and microfibers are addressed.

3. Nanofibers formation mechanism

Generally speaking, the formation of titania nanotubes has been explained by the sheet roll-up mechanism. In this process the nanosheet-like features produced after thermal treatment composed of highly distorted TiO_6 octahedra are believed to be formed by scrolling up, such that the driving force gets high enough because of the saturation of the undercoordinated sites or dangling bonds. In this structure, each Ti_{4+} ion is surrounded by an octahedron of six O_2- ions, and the distortion is generated with the aid of thermal treatment and precursor seeds (Chen & Mao, 2007) and (Kukovecz et. al., 2005). According to the previous work of Bavykin et. al. (Bavykin et. al., 2006) and (Bavykin et. al., 2009), the nanotubes are believed to be thermodinamically less stable than the nanofibers due to their increased surface area and the higher stress in the crystal lattice.

Figure 1 presents a simplified scheme of the possible formation mechanism of the nanofibers: a) starting from carbon-doped titanium dioxide crystals; b) after thermal annealings at temperatures lower than 900°C, it might occur delamination and the nanosheets are dettached; c) as the driving force is increased, the hollow nanofibers are formed, being composed by the distorted TiO_6 octahedra; d) after the hydrothermal annealing performed at 1000°C , the nanofibers probably are filled in because of the –OH bonds.

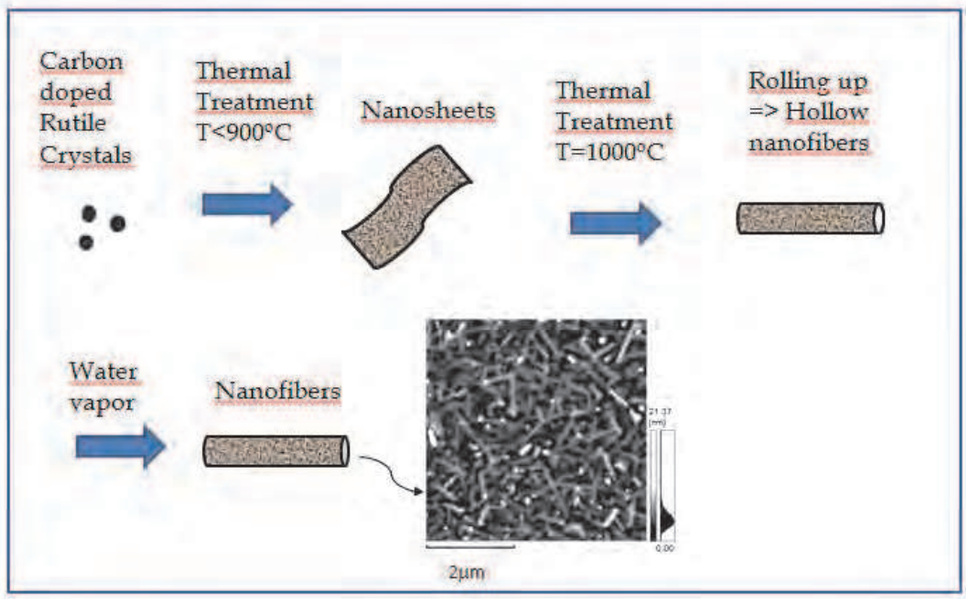

Fig. 1. The carbon doped crystals after thermal treatment are dettached in nanosheets. Increasing the temperature up to 1000°C, the sheet roll-up forming hollow nanofibers. Then, the nanofibers are filled in, probalby due to the presence of water vapor during annealing.

4. Details of sample preparation and cleaning monitoring

The initial wafer cleaning is a quite important to drop out: a) contaminant films, b) discrete particles, and c) adsorbed gases. While the RCA 1 is responsible for the organic compound dropping (such as condensed organic vapors from lubrificants, greases, photoresist, solvent residues or components from plastic storage containers), RCA 2 is responsible for the metallic (heavy metals, alkalis, and metal hydroxides) compound dropping.

Thus, a common cleaning for P-type Si (100) consists of the following sequence: a) RCA 1: 4 parts deionized (DI) water H_2O, 1 part 35% ammonium hydroxide (NH_4OH) , 1 part 30% hydrogen peroxideH_2O_2 (heated at 75°C during 15 min); b) RCA2: 4 parts DI water (H2O), 1 part 35% hydrogen chloride (HCl), 1 part 30% hydrogen peroxide (H_2O_2) (heated at 80°C during 15min) (Santos Filho et. al., 1995), (Kern, 1990) and (Reinhardt & Kern, 2008). According to S. G. Santos et. al. (Santos Filho et. al., 1995), the typical impurities found on the wafer surface analyzed by TRXFA after the conventional standard cleaning are up to 10^{10} atoms/cm^2, and the drying with the aid of isopropyl alchoholis was shown to be

efficient in removing a high percentage of particles of almost all measurable sizes (submicron and larger), as presented at table 1. Thus, after the deposition in order to perform the thermal annealings the samples were previously boiled in ultrapure isopropanol alcohol during 15 min, followed by rinsing in DI water during 5 min.
Elemental analysis were performed by using EDS technique, indicating the presence of the elements Ti, O, C or another contaminant before and after hydrothermal treatment. The EDS spectra presented show the obtained peaks for: a) as-deposited film, and b) for sample 1E (annealed at 1000ºC) where the K_α line peaks of carbon, oxygen, silicon and titanium are indicated. The L line peak of the titanium (not shown) is superimposed to the K line of the oxygen.

Element	TXRFA Convencional 10^{10} atoms/cm^2
S	<LD
K	<LD
Ca	70±30
Ti	40±20
Cr	20±10
Mn	<LD
Fe	45±8
Co	<LD
Ni	<LD
Cu	10±8
Zn	54±4

Table 1. TRXFA performed after the initial cleaning and drying at isopropyl alchoholis (Santos Filho et. al., 1995).

After the cleaning process, TiO_2 (rutile phase) and C were co-deposited on bare silicon by e-beam evaporation using the EB_3 Multihearth Electron Beam Source from Edwards and targets with 99.99% of purity from Sigma Aldrich. The carbon contents were fixed at two different concentrations: 1.5%wt or about 3.0%wt (Stem et al., 2010); (Stem et al., 2011). Then samples were boiled in a neutral ambient (isopropanol alcohol) aiming at the remotion of possible contaminants.
The deposition pressure was controlled in the range of ($2.3x10^{-6}$ – $4.6x10^{-6}$) Torr; the e-beam co-deposition current used was 150mA for a fixed time of 1min in order to produce a thickness close to 200nm.
After the co-deposition, hydrothermal annealing was performed in resistance-heated furnace with an open horizontal quartz tube; samples were introduced by a quartz boat. The temperature was adjusted in the range of 700^{0}C to 1000^{0}C for the following gases (2L/min): ultrapure N_2 or wet N_2 (0.8%H_2O), for 120min. As reported by Shannon et. al. (Shannon et. al., 1964), the presence of water can greatly promote the formation of oxygen vacancies, which increases the diffusivity of oxygen ions through TiO_2 layer and reduces diffusivity of titanium interstitials. In addition, wet inert gas plays a crucial role in triggering the much higher growth rate of titanium oxide nanowires (Liu et. al., 2010). A brief summary of the

sample preparation is presented at figure 2. In this figure, the AFM analysis of the samples just after the initial cleaning, the as-deposited film and after thermal annealing are shown. The EDS spectra of the as-deposited film and after annealing are also presented.

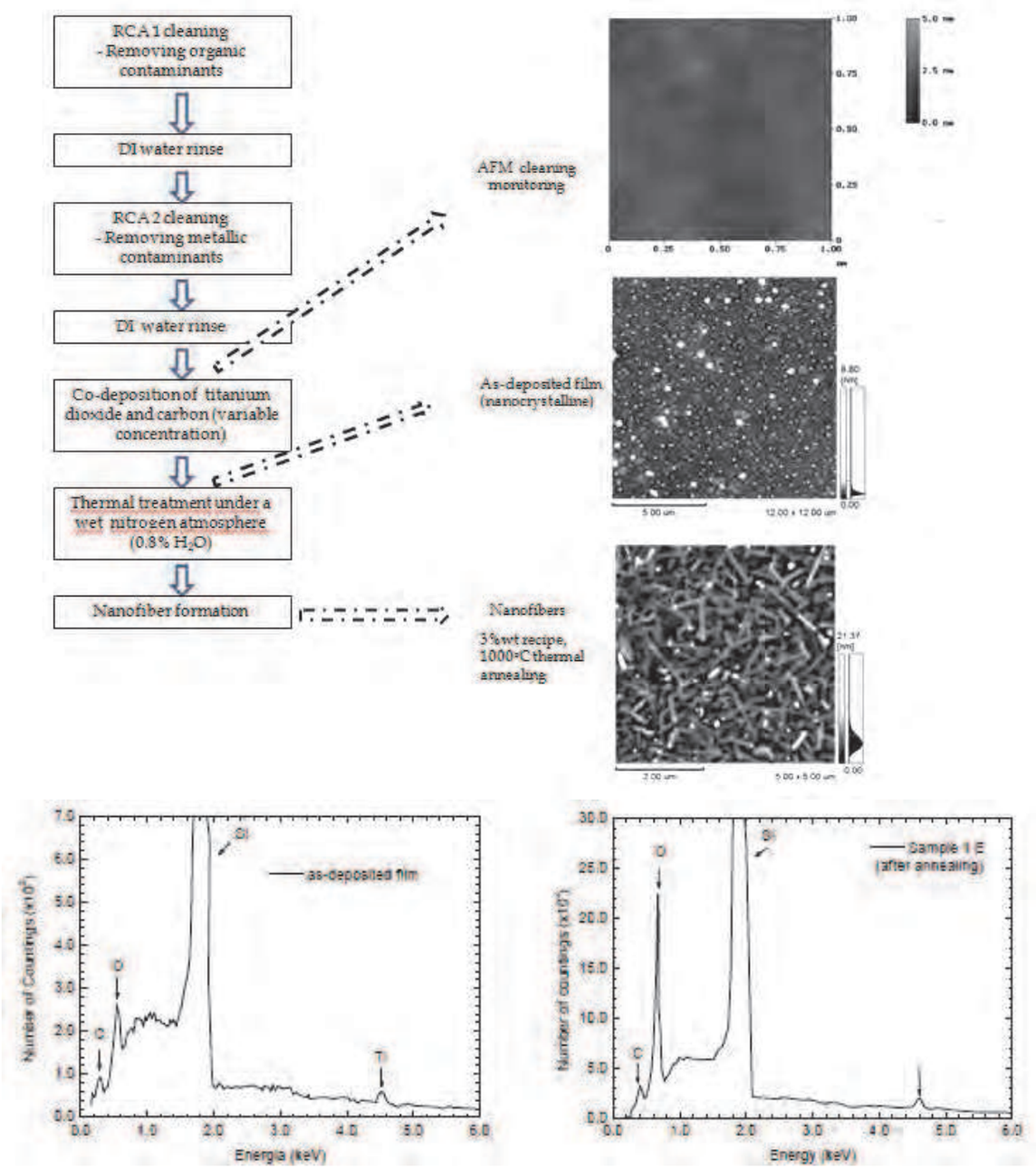

Fig. 2. Brief scheme of the sample preparation and the monitoring analysis: surface morphology by AFM technique and elemental analysis by EDS technique. The EDS spectra are not normalized; and therefore, only qualitative.

5. Producing meshes of Ti_3O_5 nano and microfibers

It is well known that is not easy to obtain titanium oxide nanowires by thermal treatment of Ti on Si, because $TiSi_2$ phases are favored over the nucleation of titanium dioxide nanowires in an inert gas or under high vacuum (Wu et. al., 2005), (Xiang et. al., 2005). In case of TiO_2 on Si, only when the high vacuum or inert gas was replaced by an oxygen-rich gas, TiO_2 nanowires could be formed on Si (Bennett et. al., 2002).

Figure 3a shows the obtained XRD spectra of titanium oxide thin films doped with 1.5%wt and 3.0%wt of carbon, respectively, and annealed at 700°C (1G), 900°C (1Fx and 1F) and 1000°C (1Ex and 1E). The annealed films are primarily amorphous with a low content of crystalline Ti_3O_5 and rutile, except for the sample 1E where the higher crystallinity is demonstrated by high intensity peaks (about 772 times higher than the lowest intensity found for sample 1G) and for sample 1G where Ti_3O_5 was not be identified. However, when temperature reaches an intermediate value for the 3%wt carbon recipe, about 900°C (as for sample 1F), the intensity of Ti_3O_5 and rutile increased in the amorphous film. On the other hand, for films doped with 1.5%wt of carbon recipe, only crystalline phase of Ti_3O_5 was observed at 700-900°C, while Ti_3O_5 and rutile are observed at 1000°C. .

Figure 3b is an ampliation of the XRD pattern shown in figure 3a of sample 1E, with the scale of the intensity reduced and, and with 2θ varying from 55 to 58 degrees when annealing to view the high intensity peaks and the peak deconvolution. It could be demonstrated that region is composed by three superposed peaks: Ti_3O_5 (<-5 1 2> and <-6 0 1>) and rutile (<220>), respectively.

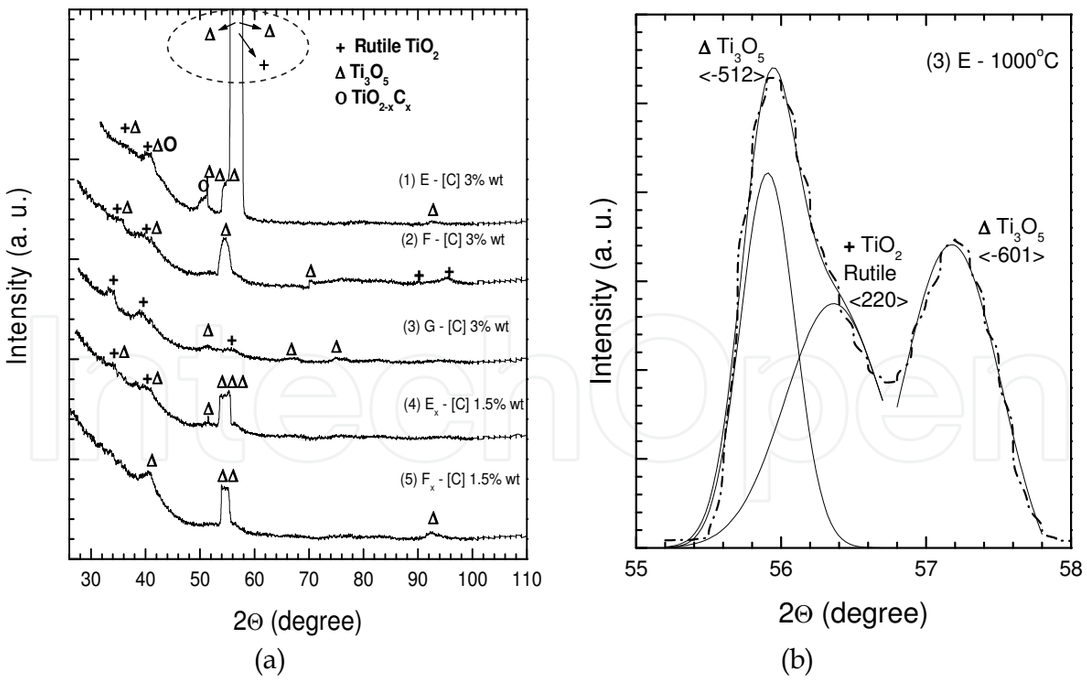

Fig. 3. (a) Typical XRD spectra for the 3%wt recipe: samples 1G (700°C), 1F (900°C) and 1E (1000°C), and for the 1.5%wt recipe: samples $1F_x$ (900°C) and $1E_x$ (1000°C); (b) ampliation of the most intense peaks of sample 1E (1000°C) (dashed region of figure 3 a) and peak deconvolution, detailing the superposed peaks.

All of the crystalline orientations for Ti_3O_5 fitted well with the XRD patterns of λ-Ti_3O_5 (Monoclinic, C2/m E, a = 9.757Å, b = 3.802Å, c = 9.452Å) (Grey & Madsen, 1994). In addition, $TiO_{2-x}C_x$ was also identified with the aid of XRD powder patterns , which is an evidence that carbon occupies positions in the crystalline phase of the titanium dioxide (interstitial and substitutional) and introduces defects, electron and hole trapping centers because of the presence of carbon and carbonate-type species (Reyes-Garcia et. al., 2008). Therefore, after annealing at 1000^{0}C (sample 1E), the structure becomes predominantly crystalline, being formed by λ-Ti_3O_5 and rutile with carbon incorporation.

In order to shed further light on the influence of the carbon content, film morphology was evaluated by dynamic mode technique (AFM of Shimadzu). Figure 4 shows the obtained AFM images of nano- and micro-fibers prepared by annealing at different temperatures in wet N_2 (0.8%H_2O) for 3 wt%-doped TiO_2 thin films on a silicon substrate: a) top view of sample 1G; b) the correspondent statistics performed for figure 5 a); c) top view of sample 1F; d) top view of sample 1E; e) 3D view of sample 1E and (f) the correspondent statistics for figure 4d.

As a result of the performed analysis, the average RMS roughness of the as-deposited film was (2.3±0.5)nm and increased to (10±2)nm after annealing at 700^{o}C in nitrogen+water vapor, being about four times higher. The observed "islands", as shown in Figure 4(a), presenting a diameter range of 19.05nm and 158.6nm.

On the other hand, as the temperature increases to 900^{o}C, a threshold temperature, the morphology starts evoluting from small "islands" to micro scale meshes of fibers, with length varying from 0.79μm to 2.06μm and widths lower than 0.400μm (range: 0. 100 to 0.400μm). In this case, the RMS roughness decreased to (5.8±0.7)nm (Figure 4(c)) and, in place of "islands", needle-like nanofibers and embedded fibers were formed on the surface and below it.

Finally, after annealing at 1000^{o}C, the film morphology was completely changed, as shown in Figure 4d (top view) and in figure 4e (3D view). In this case, micro scale meshes of fibers randomly distributed were observed with length ranging from 0.1 to 1.1μm (shown in figure 4 f) and average width of (0.170±20) μm. Also, the average RMS roughness decreased from (5.8±0.7)nm to (3.3±0.2)nm.

In contrast, when the carbon concentration was decreased below 2%wt, nano- and microfibers were not observed (AFM images not shown) on the samples prepared by annealing at different temperatures (700-1000^{0}C) in pure N_2 or wet N_2 (0.8%H_2O).

Figure 5a shows the FTIR analysis of C-doped TiO_2 samples1.5%wt ($1F_x$ and $1E_x$) and 3.0%wt (1G, 1F and 1E) that have been annealed at 700^{o}C, 900^{o}C and 1000^{o}C. A broad absorption peak at 1096cm^{-1} and this peak represents Si-O-Si stretching bond, while the Si-O-Si bending peak is also shown at 820cm^{-1} (Yakovlev et. al., 2000) and (Erkov et. al., 2000), both can be associated to silicon oxidation during the thermal annealing in water vapor atmosphere. Also, Ti-O-Ti stretching vibration of the rutile phase was observed at 614.4cm^{-1} for all samples (Yakovlev et. al., 2000) and (Erkov et. al., 2000), corroborating the XRD analysis, where a change in the cristallinity was demonstrated, evoluting from an armophous structure to a crystalline one (rutile). The higher intensity of this band is likely to be due to the increase in the amount of rutile when the carbon content is higher (3%wt). For this carbon content, Ti-O stretching at 736.5cm^{-1} (Yakovlev et. al., 2000) progressively increases as the annealing temperature increases from 700^{o}C to 1000^{o}C, which indicates progressive transition from an amorphous TiO_2 to a crystalline structure of λ-Ti_3O_5 and rutile. In addition, a band is observed at 781 cm^{-1} only for sample 1E, which was annealed at 1000^{o}C, as shown in detail in figure 5b. Richiardi et al.(Richiardi et. al., 2001) shows this

band to be due to symmetric stretching of Ti-O-Si and Si-O-Si bonds, which corroborates a quantitative mixture of SiO_2 and TiO_2 at the interface; where TiO_2 is more likely rutile since it is at the interface as established by Raman analysis (not shown).

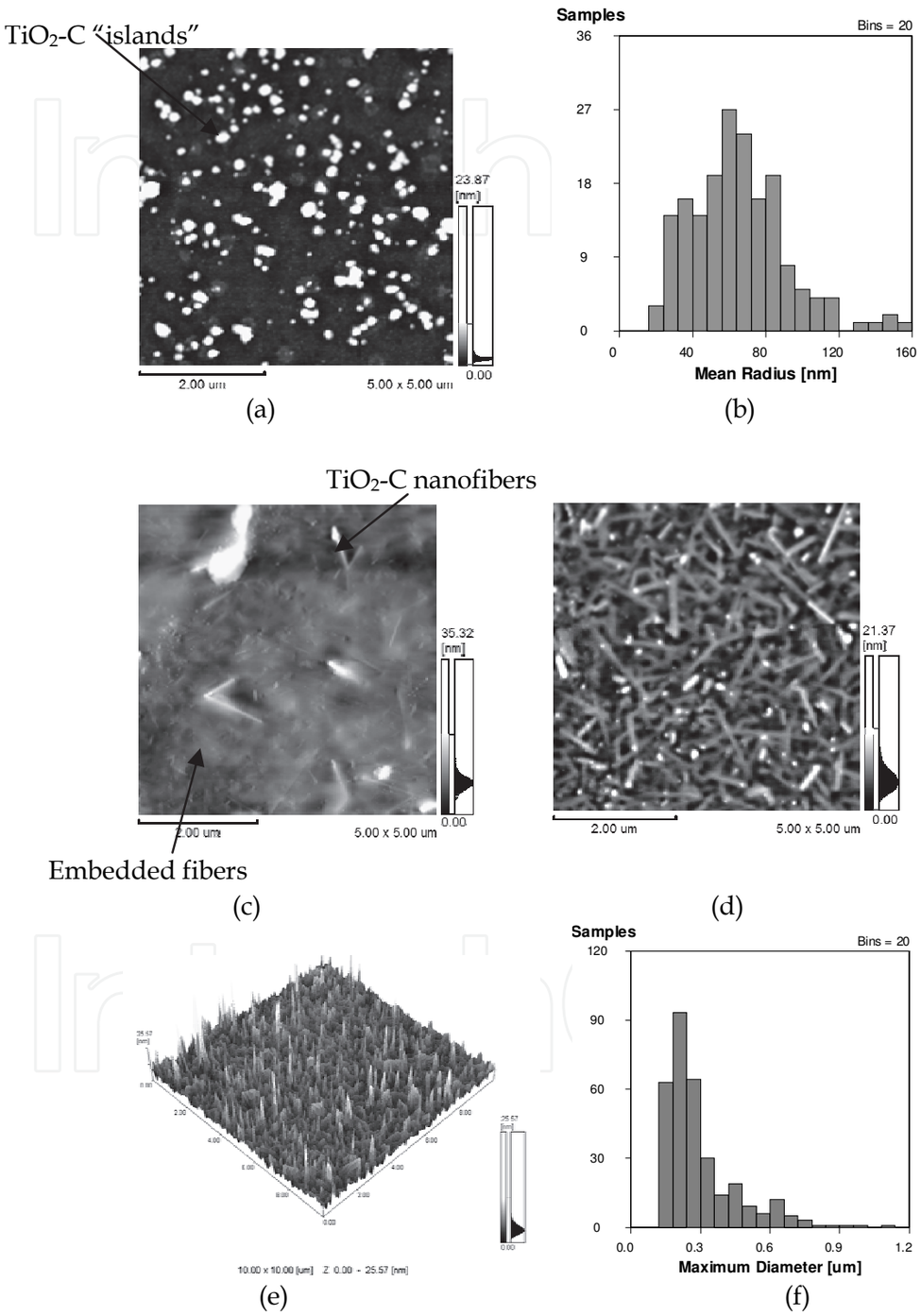

Fig. 4. Typical dynamic-mode AFM images for: (a) sample 1G annealed at 700°C; (b) statistics of (a); (c) sample 1F annealed at 900°C; (d) sample 1E (top view); (e) sample 1E (3D view) and (f) statistics of (d).

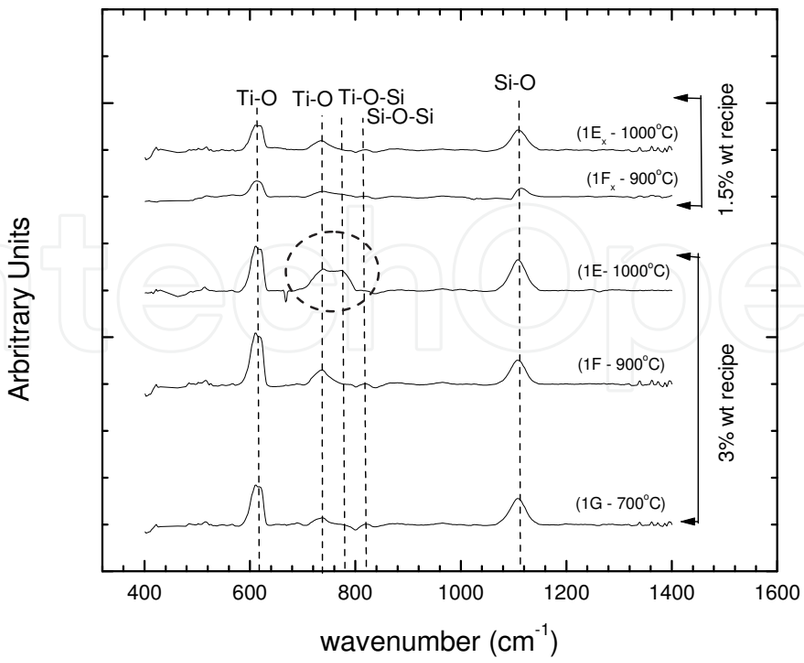

(a)

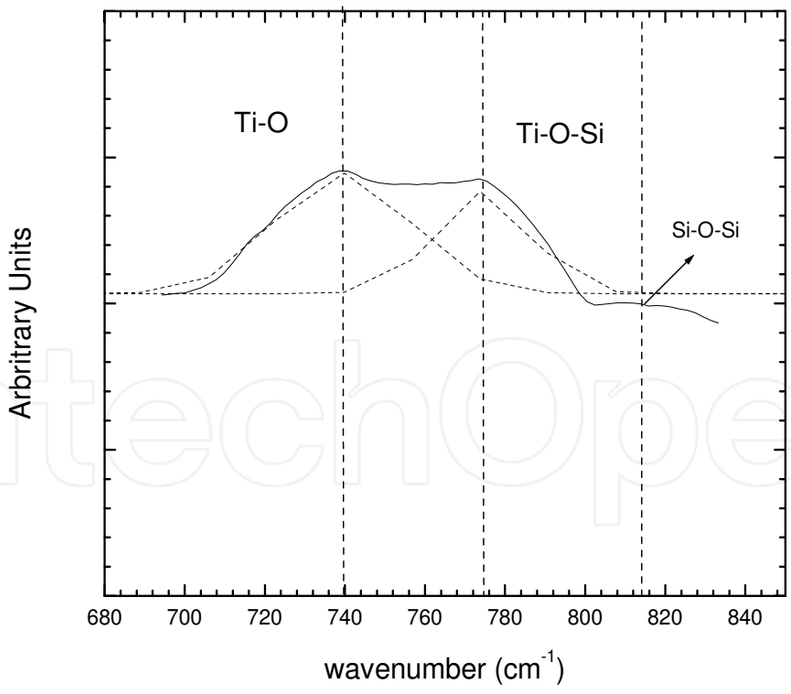

(b)

Fig. 5. a) Typical FTIR spectra as function of the wave number for the 3%wt recipe: samples 1G (700°C), 1F (900°C) and 1E (1000°C), and for the 1.5%w recipe: samples $1F_x$ (900°C) and $1E_x$ (1000°C) and b) larger view of FTIR curve.

Aiming to evaluate stoichiometry and the carbon content after thermal treatments, the aerial concentrations of oxygen and titanium were obtained from Rutherford Backscattering Spectrometry (RBS) by fitting rump-code simulation (Climent-font et. al., 2002) to the experimental spectra. Using the extracted aerial concentrations (cm^{-2}), stoichiometry of the titanium oxide was determined admitting a weighted composition of $a TiO_x + b SiO_2$, where a, b and x are calculated parameters. The carbon content was obtained by EDS analysis because the detection limit was lower than the value reported to RBS analysis (Wuderlich et. al., 1993). Also, EDS has sufficient sensitivity to distinguish carbon content of 1.5%wt from 3.0wt% (detection limit of about 0.1wt%) analysis (Wuderlich et. al., 1993). Figure 6 illustrates the experimental RBS spectrum and the fitted simulation for the sample 1E.

Table 2 presents the average concentration of carbon [C], the stoichiometry and the aerial silicon-oxide concentration [SiO_2] extracted from the EDS and RBS analyses according to the procedure described in the experimental section.

For the 3.0%wt carbon concentration in table 2, the SiO_2-layer thickness ranged from 16.2 nm (≈$7.5x10^{16}$ atoms/cm^2) to 19.4 nm (≈$9.0x10^{16}$ atoms/cm^2) for temperatures varying from 700°C to 1000°C. In this case, as predicted by the band at 1096 cm^{-1}, the higher the temperature, the higher the aerial silicon oxide concentration, which is consistent with the increase of the band at 1096 cm^{-1} in Figure 5. However, the oxygen stoichiometric coefficient of TiO_x decreased from 2.0 to 1.7 (see table 1) when the temperature was increased from 700 to 900°C. Assuming the presence of crystalline Ti_3O_5 and rutile, as illustrated by the XRD results, $TiO_{1.70}$ fits well with 25% TiO_2 and 75% Ti_3O_5 at 1000°C. Moreover, TiO_2 is consistent with predominantly amorphous TiO_2 at 700°C (sample 1G), as illustrated by the XRD results. Finally, $TiO_{1.85}$ (sample 1F) fits well with 75% TiO_2 and 25% Ti_3O_5 at 900°C (sample 1F) and is also consistent with a predominantly amorphous TiO_2, as illustrated by the XRD results.

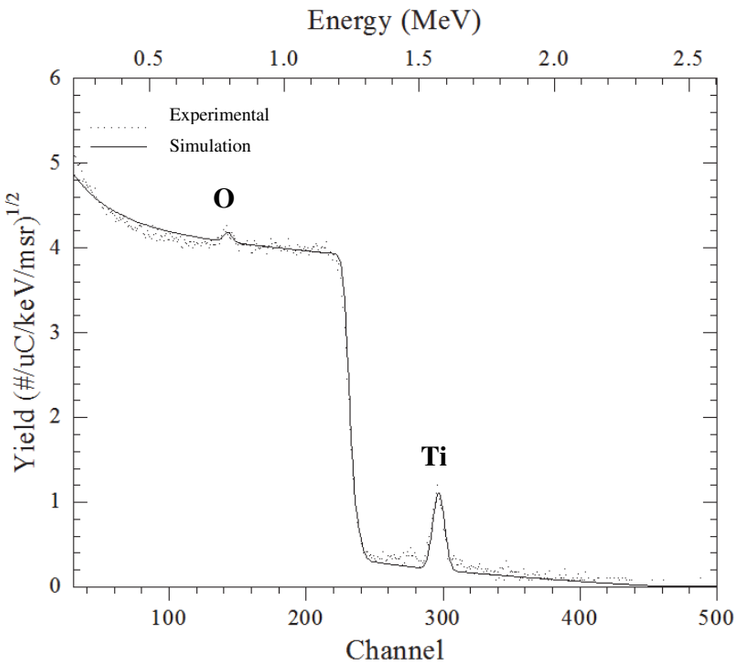

Fig. 6. Typical RBS spectrum of the sample 1E (3%w recipe).

For the 1.5%wt carbon concentration in table 2 the oxygen stoichiometric coefficient is close to 1.80 for the thermal treatments of 900°C and 1000°C. In this case, $TiO_{1.80}$ fits well with 66% TiO_2 and 33% Ti_3O_5, which is consistent with a predominantly amorphous TiO_2 with a low concentration of Ti_3O_5, as illustrated by the XRD results. In the latter case (sample 1Ex), the diffusion of the oxygen species might have been prevented, if compared to sample 1E, possibly due to a denser bulk of TiO_2 at 1000°C, which might have also slightly decreased the growth rate of the SiO_2 layer (Koch, 2002) .

Recipe	**Sample**	**Temperature** (°C)	**[C] (%wt)**	**Stoichiometry**	$[TiO_x]$ $(10^{16}/cm^2)$	$[SiO_2]$ $(10^{16}/cm^2)$
3.0%wt	1G	700	3.4±1.2	$TiO_{2.00}$	4.3	7.5
	1F	900	3.2±0.9	$TiO_{1.85}$ = $0.75TiO_2 + 0.25\ Ti_3O_5$	7.0	8.0
	1E	1000	3.4±0.6	$TiO_{1.70}$ $=0.25TiO_2 + 0.75\ Ti_3O_5$	5.7	9.0
1.5%wt	$1F_X$	900	1.5±0.4	$TiO_{1.80}$ = $0.66TiO_2 + 0.33\ Ti_3O_5$	4.3	8.0
	$1E_X$	1000	1.7±0.2	$TiO_{1.80}$ = $0.66TiO_2 + 0.33\ Ti_3O_5$	3.6	8.5

Table 2. Average concentration of carbon [C] as obtained from EDS and, stoichiometry and aerial silicon oxide concentration $[SiO_2]$ after fitting rump-code simulation to the experimental spectra using weighted compositions of $aTiO_x + bSiO_2$. TiOx layer is divided into two different layers rutile TiO_2 and Ti_3O_5 according to XRD spectra from figure 3, except for sample G where rutile TiO_2 is dominant.

Figures 7a and 7b show the diffuse reflectance spectra and the solar spectrum for AM1.5G (ASTMG173) (Stem, 2007) and (ASTM, 2005), respectively. Figure 7a allow to infer that it is evident that the film annealed at 700°C has a less significant amount of absorption in the visible region with the absorption band limited at a wavelength below 460 nm. In this case, titanium oxide is predominantly amorphous, and the literature corroborates this limited band below 460 nm (Wang et. al., 2007). However, when the annealing temperature was increased to 900°C or 1000°C, samples 1F and 1E adsorbed a much larger light fraction in the visible region, which can be attributed to a structural change of the samples associated with a phase transition to rutile, $TiO_{2-x}C_x$ and Ti_3O_5. In this case, both positions, substitutional and interstitial, carbon significantly impacts the optical properties in the range of 500 to 800 nm because of the formation of complex midgap states (Reyes-Garcia et. al., 2008) and (Wang et. al., 2007).

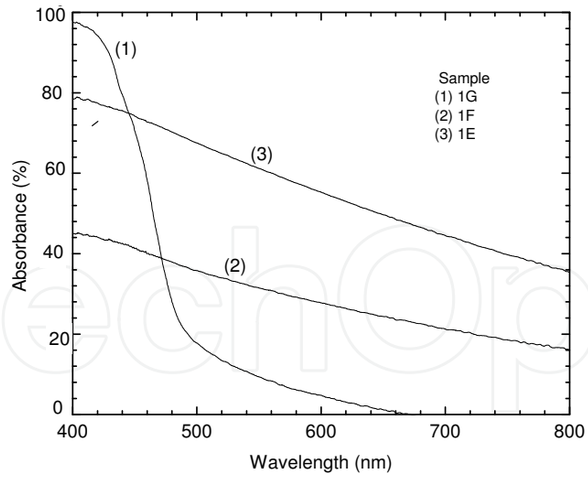

(a)

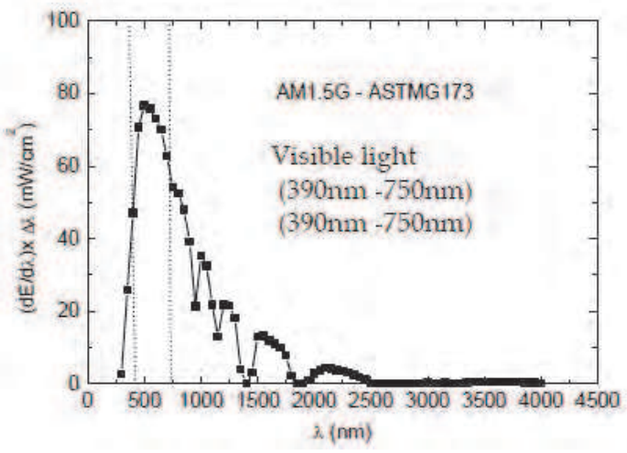

(b)

Fig. 7. (a) Absorbance curves as function of wavelength for samples processed with the 3%wt carbon recipe (1G, 1F and 1E). Their correspondent optical band-gap extracted from the curve is also presented. (b) Solar spectral irradiance as function of the wavelength, λ (nm) for AM1,5G spectrum (ASTM G173-03) (Stem, 2007), (ASTM, 2005).

Aiming at evaluating the photo catalytic properties of the developed material, the photoluminescence spectrum were obtained as function of the wavelength. Figure 8(a) shows the room temperature photoluminescence (PL) emission of the samples 1G(700°C), 1F (900°C) and 1E(1000°C) in which the vertical scale of the intensity was normalized using the silicon peak at 515nm for the three spectra. Based on this normalization, the PL emission of the samples 1G and 1F are significantly lower in area compared to sample 1E. In addition, figures 8b, 8c and 8d show the obtained spectrum for each studied case and peaks deconvolutions based on Gaussian distributions, respectively.

Basically, three characteristic band peaks are obtained: a) sample 1G: at approximately 2.2eV and 2eV; b) sample 1F: at approximately 2.2eV and 1.9eV and c) sample 1E: at approximately 2.2eV, 2.0eV and 1.9eV; which are close to one another and they are distant from the optical band gap reported on rutile (3.05eV) (Wang et. al., 2009) and on Ti_3O_5 (4.04eV) (Wouter et. al., 2007). On the other hand, Enache et al. (Enache et. al., 2004) report

that PL can reveal the nature of the defects involved in C-doped titanium oxides, showing that the broad peak at ~ 2.0eV is correlated to the amount of disorder due to the increase in the number of defects, oxygen vacancies or titanium interstitials (Enache et. al., 2004). Meanwhile, the broadband at ~1.90eV is believed to be associated to the presence of ionic point defects, or to excitons bound to these defects (Enache et. al, 2004) and the broadband at ~2.2 eV is attributed to self-trapped excitons (Enache et. al., 2004).

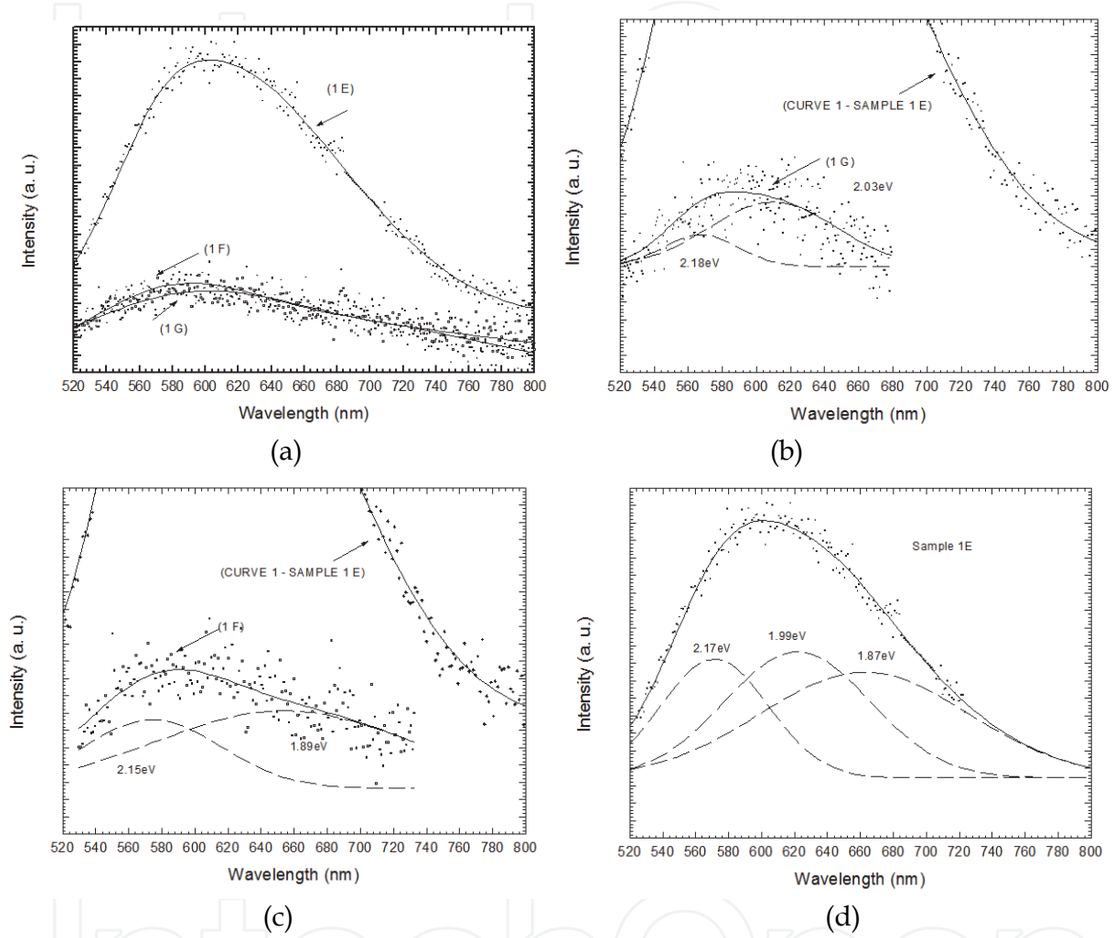

Fig. 8. PL measurements as wafunction of the wavelength: a) for the samples 1E, 1F and 1G; and peak deconvoution for samples b) 1E; c) 1F and d) 1G.

Thus, analyzing the deconvolutions (figures 8b, 8c and 8d) it can be observed that in figure 8 (b), sample G has as dominant the band centered at 2.0eV (about 63.8%) and a minor band centered at about 2.2eV, representing about 36.2% of total area. According to XRD spectra presented at figure 3a, the sample G is practically amorphous presenting small peaks associated to rutile TiO_2, thus it can be inferred that band peak at ~ 2.0eV to the number of defects, oxygen vacancies or titanium interstitials in rutile TiO_2 (as discussed item) mainly due to carbon doping and the band center at 2.2eV, attributed to some to self-trapped excitons (Enache et. al., 2004).

However, as the hydrothermal temperature annealing increases to 900°C (sample 1F), the nanofibers started to be formed, and XRD peaks corresponding to Ti_3O_5 become dominant and the band corresponding to ~ 2.0eV (tentatively associated to rutile TiO_2) practically

vanishes. In this sample, the band centered at 2.2 eV (some to self-trapped excitons) is about 35.6% of the total area, practically equal the one presented for sample 1G. Meanwhile, the start of nanofibers formation promoted the generation of a new band, compared to sample G spectrum, centered at about 1.9eV (about 64.4% of the total area) being believed to be associated to of ionic point defects, or to excitons bound to these defects (Enache et. al., 2004). These defects might be provenient from the vacancies produced by carbon doping; however, this fact needs further investigation afterwards.

As the temperature goes to 1000°C the nanofibers are formed, and two high intensity peaks were identified in XRD spectrum, rutile TiO_2 and Ti_3O_5. Analyzing the deconvolution of PL spectrum of sample 1E, three bands could be identified, being centered at 2.2eV, 2.0eV and 1.9eV, representing about 21.4%, 34.5% and 44.1% of total area, respectively. The band centered at 2.2eV, initially associated to some to self-trapped excitons in samples 1G and 1F, had its area increased significantly, about three times than for the other cases. On the other hand, the band centered at 2.0eV, that was vanished in the beginning of the nanofibers formation (sample F), became intense with the increase in the amount of disorder due to the random distribution of nano- and microfibers, which can promote increasing of the density of defects, oxygen vacancies and titanium interstitials on carbon doped rutile TiO_2 and λ-Ti_3O_5 (Monoclinic, C2/m E, a = 9.757Å, b = 3.802Å, c = 9.452Å). However, it should be pointed out that this disorder is not correlated to the cristallinity of the film as demonstrated by XRD spectra. The mentioned disorder also promoted an increase in the broadband centered at ~1.90eV, as mentioned previously, believed to be associated to the presence of ionic point defects, or to excitons bound to these defects.

In order to compare the peak areas of the studied PL spectrum, obtained based on the peak deconvolution presented at figure 8, the normalized areas for each samples are presented as functions of the characteristical band, 1.90eV, 2.00 eV and 2.20eV in figure 9. Analyzing this figure, it can be easily identified the growth of the three bands for sample 1E for the three characteristic bands.

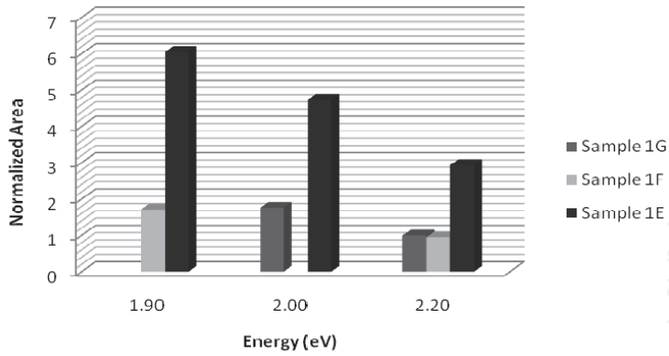

Fig. 9. Normalized areas for each studied sample as function of the normalized areas resulting from the peak deconvolution presented at figure 8.

6. Inferring about the reaction mechanisms to form the nanofibers

In order to infer a possible reaction mechanism model for producing nanofibers for the technique, the system can be divided into three groups: a) rutile carbon doped reactions; b) carbothermal reaction; c) TiO_2 behavior under nitrogen atmosphere and d) TiO_2 behavior under water vapor (an oxygen atmosphere (Richards, 2002) and hydrogen atmosphere), as presented at Table 3. The required energy to form reactions or the Gibbs potentials is

presented. Thus, the reactions that present a negative free energy are expected to occur spontaneously and the positive ones require adsorption of energy. Therefore, only the most probable or spontaneously reactions will be considered (the most negative Gibbs potential).
According to Valentini et. al.(Valentini et. al., 2005), the reactions that might occur in rutile titania and the correspondent required energy are represented for the equations (1)-(3) in table 3. Equation (1) stands for pure rutile material and (2)-(3) for carbon-doped titanium, occupying interstitial and substitutional positions, respectively. The energy required to interstitial reaction to occur is associated to the sum of the required energies to break the C-O and Ti-O bonds, while the required energy to substitutional reactions to occur is most probably associated to the tendency of carbon atoms trap electrons from the oxygen vacancy.
However, when high annealing temperatures are considered, carbothermal reactions (Sen et. al., 2011) and the interaction between TiO_2/Si (Richards, 2002) also become important. In particular, in carbothermal reaction, titanium dioxide is believed to react with carbon in order to obtain Ti_3O_5 and CO (equation (4)) in table 3. On the other hand, as the adopted atmosphere for the annealings in the proposed technique of this chapter consists of wet Nitrogen (0.8% water vapor), the dominant reactions between the interface TiO_2/Si are the ones obtained for nitrogen atmosphere, equation (5), so that Ti_3O_5 and SiO_2 are products of the expected reactions, as for the carbothermal reaction.
Focusing on the small percentage of water vapor present at the annealing atmosphere, it can be inferred that the water vapor dissociates at oxygen and hydrogen. Thus, all most probable reactions on TiO_2/Si interface point out to form Ti_3O_5, corroborating the XRD spectrum, AFM and FTIR spectra presented in the figures 3, 4 and 5.
Another point to be considered is that the hydrogen present in the atmosphere are expected to promote a kind of a redox reaction (Iowaki, 1983), when the hydrogen penetrates the film, forming oxygen vacancies and electrons are trapped as shown at equation (8). On the other hand, hydrogen is also adsorbed on neighboring oxygen, forming a hydroxyl group and Ti_3^+ that is not removed from surface, as shown in equation (9).

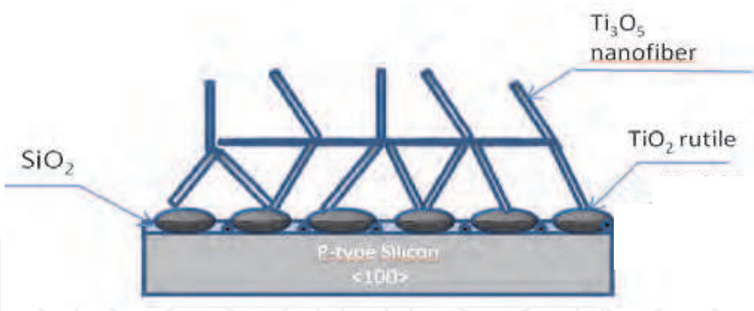

Fig. 10. Inferred scheme about nanofibers formation.

In order to understand how nano- and microfibers are formed on the silicon substrate, a schematic mechanism is proposed and illustrated in Figure 10. Initially, the amorphous TiO_2 would change from the amorphous to rutile phase, the carbon presence is believed to favor rutile phase (Binh, 2011). Rutile subsequently reacts with Si to form Ti_3O_5 (equations (4) and (5)). When the heating budget and carbon concentration are larger enough, Ti_3O_5 nano- and microfibers are formed to reach minimum free energy. The reactions presented in table 3 compete against each other to reach the minimum value for Gibbs potential, G_o. The equilibrium structure based on the competition of strain energy and surface energy would be either nanowires, or nanofibers.

Carbon doping rutile titania (Valentini et. Al., 2005)		E(eV)
	$TiO_2(s) \rightarrow TiO_{2-x}+xV_o+x/2\ O_2(g)$ (pure material) (1)	4.4
	$TiO_2C_x(s) \rightarrow TiO_{2-x}C_x(s)+xV_o+x/2\ O_2(g)$ (interstitial) (2)	2.4
	$TiO_{2-x}C_x(s) \rightarrow TiO_{2-2x}C_x(s)+xV_o+x/2\ O_2(g)$ (substitutional) (3)	2.4
Carbothermal Reactions (Sen et. al., 2011)		G_o (kJ)
	$3TiO_2 + C \rightarrow Ti_3O_5 + CO$ (4)	-156.9
TiO_2/ Si under nitrogen atmosphere (Richards, 2002)	Possible TiO_2/Si Reactions	G_o (kJ)
	$6TiO_2 + Si \rightarrow 2Ti_3O_5$ (5)	-156.9
TiO_2/ Si under oxygen atmosphere (Richards, 2002)	Possible TiO_2/Si Reactions	G_o (kJ)
	$3TiO_2+O_2 \rightarrow Ti_3O_5+3/2O_2$ (6)	398.1
	$TiO_2+O_2+Si \rightarrow TiO_2+SiO_2$ (7)	-961.5
TiO_2 under hydrogen Atmosphere (Iowaki, 1983),	$Ti^{4+}O^{2-}Ti^{4+}O^{2-} \xrightarrow{+H_2(g)} Ti^{3+}O\ Ti^{3+}O \xrightarrow{-H_2O(g)} Ti^{3+}O^{2-}Ti^{4+}\square^{-}$ (8)	
	$Ti^{3+}O^{2-}Ti^{4+}\square^{-} \overset{\frac{1}{2}H_2(g)}{\rightleftharpoons} Ti^{3+}O\ Ti^{3+}\square^{-}.$ (9) (I)	

Table 3. Possible involved reactions for the obtaining of the nanofiber.

7. Conclusions

In this chapter a review about the methods for producing nanofibers were presented and a new process for achieving the λ-Ti3O5 nano- and microfibers from C-doped TiO_2 thin films was also presented. Initially, the condition to form the nanofibers needs carbon (3%wt) as precursor seed followed by thermal treatment in nitrogen+water vapor (0.8%wt) environment at 1000°C during 120min. In this case, microscale meshes of fibers randomly distributed were observed with length ranging from 0.1 to 1.1μm and average width of (170±20)nm. The nano- and microfibers formation was characterized at different temperatures, including the initial stages at 900°C. From Raman and FTIR Spectroscopy techniques, it was shown that rutile is an inner layer located at the interface mesh/Si that is away from the surface so that the meshes of nano- and microfibers are predominantly composed of λ-Ti_3O_5 grown from the reaction with Si to form Ti_3O_5 and SiO_2. On the other hand, it was noteworthy that the microscale mesh of nano- and microfibers showed increased photoluminescence compared to amorphous TiO_2 with a broad peak in the visible

if compared with samples built up of carbon-doped rutile titanium dioxide and samples with the nanofibers at the initial stage.

8. Acknowledgements

The authors would like to thank LSI-EPUSP staff and Nelson Ordonez for the support with the E-beam equipment; Msc. André Borges Braz from LCT-EPUSP, Msc Juliana Livi Antonossi from LCT-EPUSP, Dr. Marcel D.L. Barbosa from LamFi-IFUSP and Msc. Davinson Mariano da Silva from FATEC-SP for EDS, XRD, RBS and Absorbance measurements, respectively. The FTIR measurements were performed at CCS-UNICAMP by Msc. Jair Fernandes de Souza. The authors would also like to thank Dr. Evaldo José Corat from INPE for Raman spectra discussions and, Msc Michele Lemos de Souza and Dr. Dalva Lúcia Araújo de Faria from LEM-IQUSP by the PL measurements. Nair Stem was supported by a CNPq post-doctoral scholarship under process number 151745/2008 0.

9. References

Sauvage, F; Di Fonzo, F.; Bassi, A. L.; Casari, C. S.; Russo, V.; Divitini, G.; Ducati, C.; Bottani, C. E.; Comte, P.; and Graetzel, M. (2010), Hierarchical TiO_2 Photoanode for Dye-Sensitized Solar Cells, *Nanoletters*, Vol. 10, pp 2562-2567.

Lin, H.; Wang, Wen-li; Liu, Yi-zhu and Li, Jian-bao (2009). Review article: New Trends for Solar Cell Development and Recent Progress of Dye Sensitized Solar Cells, Frontiers of Materials Science in China, Vol. 3, Nº 4, pp. 345-352.

Kim, H.; Bae, S. and Bae, D., (2010) Synthesis and Characterization of Ru Doped TiO_2 Nanoparticles by A Sol-Gel and A Hydrothermal Process, *Advances in Technology of Materials and Materials Processing*, Vol. 12, Nº 9, pp 1-6.

Wenger, S. (2010) Strategies to optimizing dye-sensitized solar cells: organic sensitizers, tandem device structures, and numerical device modeling, Ph. D. Thesis, École Polytechnique Fédérale de Lausanne.

Kong, F.; Dai, S., and Wang, K. (2007); Review of recent progress in Dye-sensitized solar cells, *Advances in OptoElectronics*, Vol. 2007, pp. 1-13.

Hafez, H.; Lan, Z.; Li, Q.; Wu, J. (2010); Review: High efficiency dye-sentized solar cell based on novel TiO_2 nanorod/nanoparticle bilayer electrode. *Nanotechnology, Science and Applications*, Vol. 3, Nº 1, pp. 45-51.

Pagliaro, M.; Palmisano, G. and Ciriminna, R. (2009); Working principles of dye-sensitized solar cells and future applications *Photovoltaics International journal*, Vol. 2, pp. 47 – 50.

Fieggemeier, E. and Hagfeldt, A. (2004), Are dye sensitized nano-structured solar cells stable? An overview of device testing and component analyses, *International Journal of Photoenergy*, V. 06, pp. 127-140.

Wang, P.; Zakeeruddin, S. M.; Moser, J. E.; Nazeeruddin, M. K.; Sekiguchi, T. and Gratzel, M., (2003). A stable quasi-solid-state dye-sensitized solar cell with an amphilic ruthenium sensitizer and polymer gel electrolyte. *Nature Materials*, Vol. 2, pp. 402-407.

Ou, Hsin-Hung and Lo, Shang-Lien (2007) Review of titania nanotubes synthesized via the hydrothermal treatment: Fabrication, modification, and application. *Sep Purif Technol,* Vol. 58, pp 179–191.

Suzuki Y and Yoshikawa S. (2004). Synthesis and thermal analyses of TiO_2-derived nanotubes prepared by hydrothermal method. *Journal of Materials Research*, Vol.. 19, pp. 982-985.

Kim, I.; Gwak, J.; Han, S.; Singh, K. (2007), Synthesis of Pd or Pt/titanate nanotube and its application to catalytic type hydrogen gas sensor, *Sensors and Actuators B,* Vol. 128, pp. 320-325.

Varghese, O. K.; Gong, D.; Paulose, M.; Ong, K. G. Mand Grimes, C. A., (2003), Hydrogen sensing using titania nanotubes, *Sensors and Actuators B*, Vol. 93, pp. 338-344.

Chen, X. and Mao, S. S. (2007), Titanium Dioxide Nanomaterials: Synthesis, Properties, Modifications, andApplications,*Chem. Rev*., Vol. 107, pp. 2891-2959.

Nuansing, W.; Ninmuang, S.;Jaremboon, W.; Maensiri, S.; Seraphin, S. (2006), Structural characterization and morphology of electrospun TiO_2 nanofibers, *Materials Science and Engineering B*, Vol. 131, Nº 1-3, pp. 147-155.

Park, S. J.; Chase, G. G.; Jerong, K. and Kim, H. Y. (2010), Mechanical Properties of titania nanofiber mats fabricated by electropsinning of sol-gel precursor, *J. Sol-gel Technol.*, Vol. 54, pp. 188-194.

D. Valentini, D.; Pacchioni, G.; Selloni, A. (2005), Theory of carbon doping of titanium dioxide, *Chem. Matter*., Vol 17, pp. 6656-6665.

Kukovecz, A.; Hodos, M.; Horváth, E. ; Radnóczi, G.; Kónya, Z.; and Kiricsi, I. (2005). Oriented Crystal Growth Model Explains the Formation of Titania Nanotubes, *The Journal of Physical Chemistry B Letters*, Vol. 109, Nº 38, pp. 17781–17783.

Puma, G. L.; Bono, A.; Krishnaiah, D.; Collin, J. G. (2008). Preparation of titanium dioxide photocatalyst loaded onto activated carbon support using chemical vapor deposition: A review paper, *Journal of Hazardous Materials*, Vol. 157, Nº 2-3, pp. 209-219.

Yamamoto, S.; Bluhm, H.; Andersson, K.; Ketteler, G.; Ogasawara, H.; Salmeron, M. and Nilsson, A. (2008); In situ x-ray photoelectron spectroscopy studies of water on metals and oxides at ambient conditions; *Journal of Physics: Condensed Matter*, Vol. 20, No 18, pp. 184025.

Khan, MA; Han, DH; Yang, OB (2009). Enhanced photoresponse towards visible light in Ru doped titania nanotube. *Applied Surface Science*. Vol. 255, pp. 3687-3690.

Zhang, H.; Li, X. and Chen, G. (2010); chapter Fabrication of Photoelectrode Materials, Electrochemistry for the Enviroment, Springer New York, ISBN 978-0-387-68318-8, pp. 475-513.

Reyes-Garcia, A.; Sun, Y.; Reyes-GLL , K. R. and Raftery, D. (2009), Solid-state NMR and EPR analysis of carbon doped titanium dioxide photocatalystis ($TiO_{2-x}C_x$), *Solid State Nuclear Magnetic Resonance in Catalysis*, Vol. 35, Nº 2, pp. 74-81.

Konstantinova, E. A.; Kokorin, A. I.; Saktivel, S.; Kisch, H. and Lips, K. (2007); Carbon-doped titanium dioxide: visible light photocatalysis and EPR investigation; *Transformation and storage of solar Energy*, Vol. 61, Nº 12, pp. 810-814.

Suzuki Y and Yoshikawa S. (2004). Synthesis and thermal analyses of TiO_2-derived nanotubes prepared by hydrothermal method. *Journal of Materials Research*, Vol.. 19, pp. 982-985.

Chen, Huei-Siou; Su, C.; Chen, Ji-Lian; Yang, Tsai-Yin; Hsu, Nai-Mu; and Li, Wen-Ren (2011), Preparation and Characterization of Pure Rutile TiO_2 Nanoparticles for Photocatalytic Study and Thin Films for Dye-sensitized Solar cells, *Journal of nanomaterials*, Vol. 2011, Nº 1, pp. 1 – 8.

Wu, Z.; Dong, F.; Zhao, W.; Wang, H.; Liu, Y. and Guan, B. (2009); The fabrication and characterization of novel carbon doped TiO_2 nanotubes, nanowires and nanorods with high visible light photocatalytic activity; *Nanotechnology*, Vol. 20, No 23, p. 235701.

Tryba, B. (2008), Increase of the photocalaytic activity of TiO_2 by carbon and iron modifications – review article, International Journal of Photoenergy, Vol. 2008, Article ID 721824, pp.1-15.

Dai, Z. R.; Gole, J. L.; Stout, J. D. and Wang, Z. L. (2002), Tin Oxide Nanowires, Nanoribbons, and Nanotubes; *J. Phys. Chem. B,* Vol. 106, Nº 6, pp 1274–1279.

Yin, Y.; Zhang, G. and Xia, Y. (2002), Synthesis and Characterization of MgO Nanowires through a Vapor-Phase Precursor Method, *Adv. Func. Mater.*, Vol. *12*, pp.293-298.

Pan, Z. W., Dai, Z.R., and Wang, Z.L. (2002), Lead oxide nanobelts and phase transformation induced by electron beam irradiation, *Appl. Phys. Lett.*, Vol. 80, pp. 309-311.

Wu, J. M.; Shin, H. C. and Wu, W. T. (2005), Growth of TiO_2 nanorods by two-step thermal evaporation, *J. Vac. Sci. Technol. B*, Vol. 23, pp. 2122 – 2126.

Xiang, B., Wang, Q. X.; Zhang, X. Z.; Liu, L. Q.; Xu, J. and Yu., D. P. (2005), Synthesis and field emission properties of $TiSi_2$ nanowires *Appl. Phys. Lett. 86*, pp. 243103/1-243103/3 issue 24

Bennett, P. A.; Ashcroft, B.; He,Z. and Tromp, R. M. (2002), Growth dynamics of titanium silicide nanowires observed with low-energy electron microscopy, *J. Vac. Sci. Technol. B*, Vol. 20, pp. 2500-2504.

Wang, C. C.; Yu, C.-Y.; Kei, C. C.; Lee, C. T. and Perng, T. P. (2009); Formation of TiO_2 nanowires on silicon directly from nanoparticles, *Nanotechnology*, Vol. 20, pp. 1-6.

Sen, W.; Xu, B. q.; Yang, B.; Sun, H.-y.; Song, J.-x.; Wan, H.-l. and Dai, Y.-n. (2011), Preparation of TiC powders by carbothermal reduction method in vacuum, *Transactions of Nonferrous Metals Society of China* , Vol. 21, Nº 1, pp 185-190.

Swift, G. A. and Koc, R. (1999), Formation studies of TiC from carbon coated TiO_2, *Journal of Materials Science*, Vol. 34 , pp. 3083 – 3093.

Bavykin, D. V.; Friedrich, J. M. and Walsh, F. C. (2006); Protonated titanates and TiO_2 nanostructured nanomaterials: synthesis, properties and applications, Vol. 18, Nº 21, pp. 2807-2824.

Bavyjkin, D. V. and Walsh, F. C. (2009); Elongated titanate nanostructures and their applications; *European Journal of Inorganic Chemistry*, Vol. 2009, Nº 8, pp. 977-997.

Santos Filho, S. G.; Hasenak, C. M.; Sanay, L. C. and Mertens, P. (1995); A less critical cleaning procedure for silicon wafer using diluted HF dip and boiling in isopropyl alcohol as final step; *J. Eletrochemical Soc.*, Vol. 142, Nº 3, pp. 902 – 907.

Stem, N.; Santos Filho, S. G. (2010); Carbon-Modified Titanium Dioxide Deposited by E-Beam Aiming Hydrogen Sensing. *In: 25th Symposium on Micreoelectronics Technology and Devices, 2010, São Paulo. 25th Symposium on Micreoelectronics Technology and Devices (ECS Transactions*). New Jersey, USA : Pennington, Vol. 31, pp. 433-439.

Stem, N.; Chinaglia E. F.; Santos Filho, S. G. (2011); Ti_3O_5 nano- and microfibers prepared via annealing of C-doped TiO_2 thin films aiming at solar cell and photocatalysis applications. *In: 26th Symposium on Microelectronics Technology and Devices (ECS Transactions). New Jersey, USA: Pennington, 2011.*

Stem, N.; Chinaglia E. F.; Santos Filho, S. G. (2011). Microscale meshes of Ti_3O_5 nano- and microfibers prepared via annealing of C-doped TiO_2 thin films. *Materials Science & Engineering. B, Solid-State Materials for Advanced Technology*, DOI: 10.1016/ j.mseb.2011.06.013, available on line.

Kern, W. (1990); The evolution of silicon wafer technology, *The Journal of Eletrochemical Society*, Vol. 137, Nº 6, pp.1887-1892.

Reinhardt, K. A. and Wern. K (2008); Handbook of Silicon Wafer Cleaning Technology, Materials Science and Process Technology Series. 2nd Edition, Willian Andrew.

Shannon, R. D. (1964), Phase transformation studies in TiO_2 supporting different defect mechanisms in vacuum-reduced and hydrogen-reduced rutile. *J Appl Phys*, Vol. 35, pp. 3414–3416.

Liu, H.; Zhang, Y.; Li, R.; Cai, M.; Sun, X. (2010), A facile route to synthesize titanium oxide nanowires via water-assisted chemical vapor deposition *J. Nanopart. Res.* (2010) DOI 10.1007/s11051-010-0041-0.

Grey, I. E.; Li, C.; Madsen, I. C. (1994) Phase Equilibria and Structural Studies on the Solid Solution $MgTi_2O_5$-Ti_3O_5 *Journal of Solid State Chemistry*, Vol. 113, Nº 1, pp. 62-73.

Yakovlev, V. V.; Scarel, G.; Aita, C. R. and Mochizuki, S. (2000), Short-range order in ultrathinfilm titanium dioxide studied by Raman spectroscopy, *Appl. Phys. Lett.*, Vol. 76, Nº 9, pp. 1107-1109.

Erkov, V. G.; Devyatova, S. F.; Molodstova, E. L.; Malsteva, T. V.; and Yanovskii, U. A. (2000). Si-TiO_2 interface evolution at prolonged annealing in low vacuum or N_2O ambient Applied Surface Science, Vol. 166, Nº 1, pp. 51–56.

Climent-font, A; Watjen, U. and Bax, H. (2002); Quantitative RBS analysis using RUMP. On the accuracy of the He stopping in Si Nuclear Instruments and Methods in Physics Research, Section B, Vol. 71, pp. 81-86.

G. Richiardi, Al Damin, S. Bordiga, C. Lamberti, G. Spanó, F, Rivetti and A. Zecchina (2001), *J. Am. Chem. Soc.*, Vol. 123, 11409-11419.

Wuderlich, W.; Foitzik, A. H.; and Heuer, A. H. (1993); On the Quantitative EDS Analysis of Low Carbon Concentrations in Analytical TEM; *Ultramicroscopy*, Vol. 49, pp. 220 - 224.

Koch, Carl C. (2002). Nanostructured Materials - Processing, Properties and Potential Applications.. William Andrew Publishing/Noyes.New York, USA, ISBN 0-815514514.

ASTM G-173-03, Standard Table for reference solar spectrum irradiance direct normal and hemisphericalon 37º tilted surface, avaible at www.astm.org, accessed January 2005.

Stem, N. (2007), Células solares de silício de alto rendimento: otimizações teóricas e implementações experimentais utilizando processos de baixo custo, PhD Thesis, Escola Politécnica de Engenharia Elétrica da Universidade de São Paulo, http://www.teses.usp.br/teses/disponiveis/3/3140/tde-02042008-113959/fr.php.

Wang, X.; Meng, S.; Zhang, X.; Wang, H.; Zhong, W. and Du, Q. (2007). Multi-type carbon doping of TiO_2 photocatalyst, Chem. Phys. Lett., Vol. 444, pp. 292-296.

Sakthivel, S. and Kisch, H. (2003), Daylight Photocatalysis by Carbon-Modified Titanium Dioxide. *Angewandte Chemie International Edition*, Vol. 42, Nº 40, pp. 4908–4911.

Wouters, Y.; Galerie, A. and Petit, J-P. (2007), Photoelectrochemical study of oxides thermally grown on titanium in oxygen or water vapor atmospheres, *Journal of the Electrochemical Society*, Vol. 154, Nº 10, pp. C587-C592.

Enache, C. S.; Schoonman, J. S. and De Krol, R. V. (2004), The Photoresponse of Iron- and Carbon-Doped TiO_2 (Anatase) Photoelectrodes, *J. Electroceramics*, Vol. 13, Numbers 1-3, pp. 177-182.

Richards, B. S. (2002), Novel Uses of Titanium Dioxide for Silicon Solar Cells, *Ph.D. Thesis*, University of New South Wales.

Iowaki, T. (1983). Studies of the surface of titanium dioxide. Part 5.—Thermal desorption of hydrogen, *J. Chem. Soc., Faraday Trans. 1*, Vol. 79, pp. 137-146.

Dang, Binh H.Q.; Rahman, Mahfujur; MacElroy, J. M. Don (2011). Conversion of amorphous TiO_2 coatings into their crystallineform using a novel microwave plasma treatment. *Surface and Coatings Technology*, Article in Press

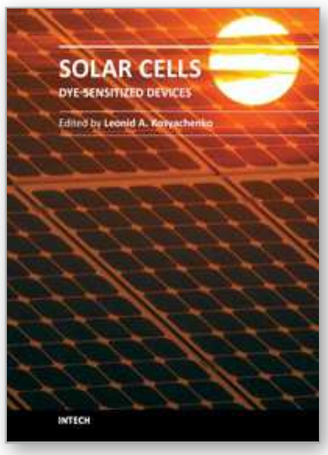

Solar Cells - Dye-Sensitized Devices

Edited by Prof. Leonid A. Kosyachenko

ISBN 978-953-307-735-2
Hard cover, 492 pages
Publisher InTech
Published online 09, November, 2011
Published in print edition November, 2011

The second book of the four-volume edition of "Solar cells" is devoted to dye-sensitized solar cells (DSSCs), which are considered to be extremely promising because they are made of low-cost materials with simple inexpensive manufacturing procedures and can be engineered into flexible sheets. DSSCs are emerged as a truly new class of energy conversion devices, which are representatives of the third generation solar technology. Mechanism of conversion of solar energy into electricity in these devices is quite peculiar. The achieved energy conversion efficiency in DSSCs is low, however, it has improved quickly in the last years. It is believed that DSSCs are still at the start of their development stage and will take a worthy place in the large-scale production for the future.

INTECH
open science | open minds

InTech Europe
University Campus STeP Ri
Slavka Krautzeka 83/A
51000 Rijeka, Croatia
Phone: +385 (51) 770 447
Fax: +385 (51) 686 166
www.intechopen.com

InTech China
Unit 405, Office Block, Hotel Equatorial Shanghai
No.65, Yan An Road (West), Shanghai, 200040, China
中国上海市延安西路65号上海国际贵都大饭店办公楼405单元
Phone: +86-21-62489820
Fax: +86-21-62489821

IntechOpen